MNRAS **000**, 000–000 (0000) Preprint 8 July 2020 Compiled using MNRAS LATEX style file v3.0

Inverse-Compton scattering in the resolved jet of the high-redshift quasar PKS J1421-0643

D.M. Worrall[1], M. Birkinshaw[1], H.L. Marshall[2], D.A. Schwartz[3], A. Siemiginowska[3] and J.F.C. Wardle[4]

[1]*HH Wills Physics Laboratory, University of Bristol, Tyndall Avenue, Bristol BS8 1TL, UK*
[2]*Kavli Institute for Astrophysics and Space Research, MIT, 77 Massachusetts Avenue, Cambridge, MA 02139, USA*
[3]*Harvard-Smithsonian Center for Astrophysics, 60 Garden Street, Cambridge, MA 02138, USA*
[4]*Department of Physics, Brandeis University, 415 South Street, Waltham, MA 02454, USA*

8 July 2020

ABSTRACT

Despite the fact that kpc-scale inverse-Compton (iC) scattering of cosmic microwave background (CMB) photons into the X-ray band is mandated, proof of detection in resolved quasar jets is often insecure. High redshift provides favourable conditions due to the increased energy density of the CMB, and it allows constraints to be placed on the radio synchrotron-emitting electron component at high energies that are otherwise inaccessible. We present new X-ray, optical and radio results from *Chandra*, *HST* and the *VLA* for the core and resolved jet in the $z = 3.69$ quasar PKS J1421-0643. The X-ray jet extends for about 4.5″ (32 kpc projected length). The jet's radio spectrum is abnormally steep and consistent with electrons being accelerated to a maximum Lorentz factor of about 5000. Results argue in favour of the detection of inverse-Compton X-rays for modest magnetic field strength of a few nT, Doppler factor of about 4, and viewing angle of about 15°, and predict the jet to be largely invisible in most other spectral bands including the far- and mid-infrared and high-energy gamma-ray. The jet power is estimated to be about 3×10^{46} erg s^{-1} which is of order a tenth of the quasar bolometric power, for an electron–positron jet. The jet radiative power is only about 0.07 per cent of the jet power, with a smaller radiated power ratio if the jet contains heavy particles, so most of the jet power is available for heating the intergalactic medium.

Key words: galaxies: active – galaxies: jets – quasars: individual: PKS J1421-0643– radiation mechanisms: non-thermal – radio continuum: galaxies – X-rays: galaxies

1 INTRODUCTION

A key finding with *Chandra*, only possible due to its spatial fidelity and sensitivity, has been the detection of kpc-scale X-ray jets in quasars (Tananbaum et al. 2014). Following the discovery of a jet during the initial *Chandra* focussing operations (Schwartz et al. 2000), several quasar jet surveys have been conducted, normally with individual exposures in the range 5 to 20 ks, targeting quasars mostly at low redshift, $z \lesssim 1$, with jets well mapped in the radio (Sambruna et al. 2002, 2004, 2006; Marshall et al. 2005, 2011, 2018; Jorstad & Marscher 2006; Hogan et al. 2011). While all the quasar cores are X-ray detected, the X-ray detection rate for at least one resolved jet knot is also high, at roughly 60 per cent. Some *Chandra*-discovered jets have had follow-up observations to study X-ray morphology and spectral properties, the deepest exposures (> 100 ks) being for PKS 1127-145 and 4C+19.44 (Siemiginowska et al. 2007; Harris et al. 2017).

The X-ray emission mechanism of these low-redshift quasar jets is surprisingly hard to ascertain, and remains a subject of heated debate, having profound implications for the kinetic power of the jets or the acceleration process, or both (see Worrall 2009). As in nearby 3C 273, at $z = 0.158$, whose kpc X-ray jet was known before *Chandra* (Willingale 1981; Röser et al. 2000), there are good arguments for believing synchrotron emission dominates in high-contrast knots, requiring those regions to be efficient particle accelerators to extreme energies (e.g., Jester et al. 2006; Marchenko et al. 2017). On the other hand, the high detection rate in the X-ray of radio-jetted quasars, often with optical detections or upper limits falling below spectral interpolations between radio and X-ray, would require an extraordinary jet acceleration process if from elec-

tron synchrotron radiation (e.g., Schwartz et al. 2000, 2006; Sambruna et al. 2004), and has given weight to an interpretation of inverse Compton (iC) scattering on the cosmic microwave background (CMB) (i.e., the iC-CMB mechanism, Tavecchio et al. 2000; Celotti et al. 2001). Early applications of the iC-CMB model stressed that the quasar jet must remain highly relativistic on kpc scales, such that it sees boosted CMB in its rest frame and emits beamed X-rays in the observer's frame. Modelling has tended to find beaming parameters that seem quite extreme for large distances from the core (Doppler factors in the range 5 to 20, implying high Lorentz factors and small angles to the line of sight), with no significant jet deceleration between parsec and kpc scales, sometimes out to many hundreds of kpc before subsequent jet bending (e.g., Jorstad & Marscher 2004; Tavecchio et al. 2004). The implications are high jet power, often rivalling the quasar radiative power (Schwartz et al. 2006).

Whereas X-ray synchrotron radiation requires there to be electrons of extreme (super-TeV) energy, the existence of electrons with low relativistic energies is certain, as higher-energy electrons lose energy by radio synchrotron radiation, and so iC-CMB is mandatory. The increased energy density of the CMB at high redshift should lead to proportionally more X-ray jet detections at high z (Schwartz 2002), but statistical tests that have looked for the expected $(1+z)^4$ dependency in the X-ray to radio flux ratio have failed to support an exclusive iC-CMB description without invoking additional evolutionary effects in the jets for which observational support is unproven (Marshall et al. 2011, 2018). In a similar vein, it has been argued that if resolved quasar X-ray jets at $z < 1$ are scaled with the CMB, the addition to the core emission violates observations in predicting excess quasar X-ray luminosity evolution (Miller et al. 2011) and much brighter X-ray fluxes than are found in targeted SDSS quasars at $z > 4$ (Zhu et al. 2019).

Clever approaches have been employed to test the iC-CMB model at low redshift, using *HST* optical polarization (Cara et al. 2013), or *Fermi* upper limits to constrain Compton scattering to high-energy gamma rays (Meyer & Georganopoulos 2014; Meyer et al. 2017; Breiding et al. 2017), with both disfavouring the iC-CMB model in several sources, of which some were earlier modelled as iC-CMB. It seems convincing that it is incorrect to assume that the resolved jets in low-redshift quasar jets are dominated by iC-CMB, and incorrect to use all of the measured X-ray flux to scale them to high redshift. A more promising approach is to look in depth directly at jets at high redshift, with a view to inferring their likely physical conditions and beaming parameters. Scaling to low redshift might then provide an estimate of the contribution of iC-CMB to the X-ray emission of low-redshift quasars.

A lack of jets with strong X-ray and weak radio emission has been seen as a problem for the iC-CMB model. How large a problem remains unclear, because surveys targeted to find resolved X-ray jets are biased towards quasars with strong radio jets. In a 19-ks *Chandra* exposure, Simionescu et al. (2016) found serendipitously an extended X-ray jet in the $z = 2.5$ quasar B3 0727+409, whose radio emission is point-like except for one knot 1.3″ from the core. They conclude strong support for the iC-CMB mechanism. The space density of radio-loud quasars at moderate to high redshift that have high-fidelity radio observations, coupled with the sky coverage of *Chandra*, is sufficiently low that it is not unexpected that we have failed to find additional such cases in searches of *Chandra* archival data. More recent *Chandra* targetted observations of 14 previously unobserved quasars have found two candidate X-ray jet systems where no underlying radio jet emission is seen (Schwartz et al. 2019).

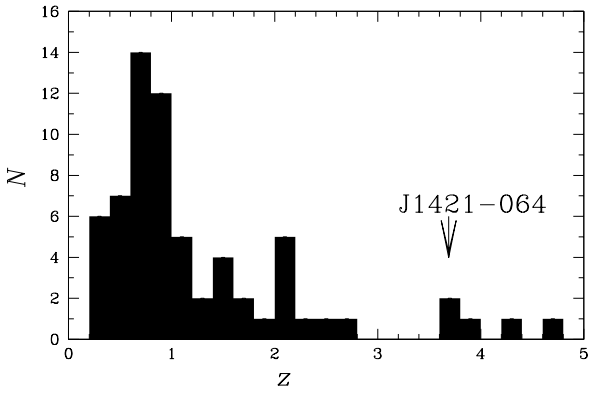

Figure 1. Redshift distribution of 66 quasars at $z > 0.2$ with detected kpc-scale X-ray jets. Objects here are in one or more of the surveys reported by Sambruna et al. (2002, 2004); Marshall et al. (2005, 2011, 2018); Jorstad & Marscher (2006); Hogan et al. (2011); McKeough et al. (2016), and eleven additional cases have been added from Schwartz et al. (2000); Chartas et al. (2002); Fabian, Celotti & Johnstone (2003); Siemiginowska et al. (2003a, 2007); Cheung, Stawarz, & Siemiginowska (2006); Miller et al. (2006); Tavecchio et al. (2007a); Miller & Brandt (2009); Saez et al. (2011); Simionescu et al. (2016). The median redshift is 0.89.

That most jet work to date has concentrated on nearby objects is seen from Figure 1 which displays a histogram (shaded) of the redshift distribution of all quasars at $z > 0.2$ for which X-ray kpc-scale jets are reported to our knowledge. Because observations must be with *Chandra* and, with the exception of B3 0727+409, were all as targets, there remain relatively few detections, particularly at medium to high redshift. However, detection rates in short exposures at the higher redshifts are high. For example, McKeough et al. (2016) summarize *Chandra* results for a sample of eleven quasars at $z > 2.1$ with resolved radio jets, five of which are at $z > 3.5$. Eight of the eleven display extended X-ray emission associated with jet features, and in seven of these cases the *Chandra* exposure times were short, between 3.3 and 20.1 ks. Three of the $z > 3.5$ sources show jet features, as do additional sources at $z = 3.89$ and $z = 3.63$ reported by Cheung et al. (2006) and Saez et al. (2011), respectively, giving the five known jet sources at $z > 3.5$ listed in Table 1. Of these five, the source with the longest X-ray jet but shortest observation time is PKS J1421-0643. We have therefore undertaken a programme of deeper observations of PKS J1421-0643, using *Chandra*, *HST*, and the *VLA*, with a view to testing the plausibility and implications of the iC-CMB process to explain its X-ray emission, and measuring the physical parameters of this high-redshift jet.

In this paper we adopt values for the cosmological parameters of $H_0 = 70$ km s^{-1} Mpc^{-1}, $\Omega_{\rm m0} = 0.3$, and $\Omega_{\Lambda 0} = 0.7$. Thus at PKS J1421-0643's redshift of $z = 3.689$ (Hook et al. 2003), 1 arcsec corresponds to a projected dis-

Table 1. Archival X-ray quasar jets at $z > 3.5$.

(1) Name	(2) z	(3) *Chandra* (ks)	(4) References
PMN J2219-279	3.63	46.0	Saez et al. (2011)
PKS J1421-0643	3.689	3.3	Cheung et al. (2008)
			McKeough et al. (2016)
4C+62.29	3.89	18.3	Cheung et al. (2006)
GB 1508+5714	4.3	89.0	Yuan et al. (2003)
			Siemiginowska et al. (2003b)
			McKeough et al. (2016)
GB 1428+4217	4.72	10.6	Cheung et al. (2012)
			McKeough et al. (2016)

(3) Reported *Chandra* exposure time.

Table 2. *Chandra* Observations of PKS J1421-0643.

(1) ObsID	(2) Date	(3) Frame Mode	(4) Sub-array	(5) Exposure (ks)
20445	2018 Mar 27	VFAINT	1/4	22.001
21054	2018 Mar 29	VFAINT	1/4	41.033
21055	2018 Mar 30	VFAINT	1/4	24.488
21056	2018 Mar 31	VFAINT	1/4	18.559
21057	2018 Apr 01	VFAINT	1/4	11.766
7873	2007 Jun 04	FAINT	1/8	3.342

tance of 7.18 kpc. Spectral index, α, is defined in the sense that flux density is proportional to $\nu^{-\alpha}$. In the X-ray, α relates to the modelled photon spectral index, Γ, as $\Gamma = \alpha + 1$.

2 OBSERVATIONS AND REDUCTION METHODS

2.1 *Chandra* X-ray

Our observations of PKS J1421-0643 with the S3 back-illuminated CCD of the Advanced CCD Imaging Spectrometer (ACIS) on board *Chandra* were made as given in Table 2 (ObsIDs 20445, 21054, 21055, 21056 and 21057). In addition we make use of archival data from a short observation taken with the same CCD eleven years earlier (ObsID 7873), also listed in Table 2. Details of the ACIS instrument and its modes of operation are given in the *Chandra* Proposers' Observatory Guide[1]. Results presented here use CIAO (Fruscione et al. 2006) v4.11 and the CALDB v4.8.2 calibration database. We reprocessed the data following the software 'threads' from the *Chandra* X-ray Center (CXC)[2], to make new level 2 events files, applying the sub-pixel event repositioning algorithm. VFAINT screening was not applied for the analysis here due to the small angular scale of the quasar and its jet, and the fact that such screening can remove valid events from the core.

The observations were free from large background flares and, after removal of time intervals when the background deviates more than 3σ from the average value, the total exposure time was 121.2 ks, distributed as given in Table 2. We applied small corrections to align the centroid of 1–5-keV counts from the core of PKS J1421-0643 to our measured radio core position of RA= $14^{\rm h}21^{\rm m}07\overset{\rm s}{.}756$, Dec= $-06°43'56''.36$. No observation required a shift larger than 0.17 arcsec.

Our spectral fitting used XSPEC[3] v12.10.1d. If there were more than 300 net counts in the region of interest we used the χ^2 statistic after grouping data to a minimum of 20 counts bin^{-1}; otherwise we used cstat, after binning to at least one count per bin, and where the wstat statistic gives a rough indication of goodness of fit. For absorption we used the phabs and zphabs model for Galactic and intrinsic absorption, respectively, with the abundance table of Asplund et al. (2009). PKS J1421-0643 is at a Galactic latitude of 50°, and the line-of-sight column density is given as $N_{\rm H} = 3.4 \times 10^{20}$ cm^{-2} by the CXC COLDEN routine using data of Dickey & Lockman (1990). This component of fixed Galactic absorption was included in all spectral modelling. Local background was used with exclusion regions corresponding to sources found by the CIAO WAVDETECT task. Extracted spectra and response files were combined using the CIAO COMBINE_SPECTRA task and fitted to spectral models over the 0.5 to 7-keV energy band. The ACIS response was significantly higher at low energies when the earlier short observation was made, but we find negligible change to fitted spectral shape whether or not these earlier data are included. The X-ray spectrum of the core was measured from a circle of radius 1.25 arcsec using the CIAO SPECEXTRACT task, correcting for missing counts based on the Point Spread Function (PSF) and sampling background from a source-centred annulus of radii 10 and 50 arcsec. The jet spectrum was measured using regions described in Section 3.2.

After the X-ray spectrum of the core had been modelled, we used the CXC SAOSAC RAYTRACE and MARX software to make 50 simulations of the PSF using inputs appropriate for the longest observation, ObsID 21054, including supplying the aspect solution and applying the EDSER subpixel algorithm to match the data. These were combined to provide an image of the spatial extent of the PSF which was convolved with models for spatial comparison with data.

2.2 *VLA* radio

We observed PKS J1421-0643 in programme SJ0472 for 3.5 h with the Karl G. Jansky Very Large Array (*VLA*) in its A-array configuration on 2018 March 04. Data were taken in the C and X bands, covering 3.98 to 12.02 GHz. Flux-density calibration was based on 3C 286 (J1331+3030) which also provided the polarization position angle reference. The low-polarization calibrator OQ 208 (J1407+2827) provided measurements of polarization leakage. Phase calibration used J1408-0752, which lies 3.3° from PKS J1421-0643. Calibration and mapping were performed within the CASA software.

Extensive flagging for interference was required, with

[1] http://cxc.harvard.edu/proposer
[2] http://cxc.harvard.edu/ciao
[3] https://heasarc.gsfc.nasa.gov/xanadu/xspec/

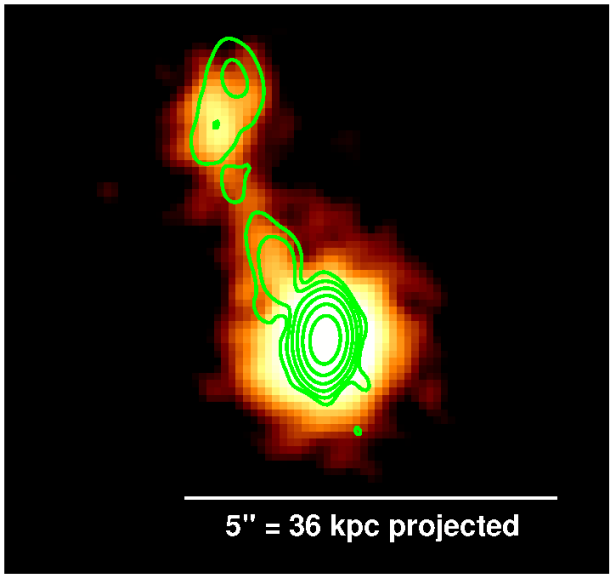

Figure 2. 0.5–5-keV *Chandra* image of PKS J1421-0643 in 0.0984-arcsec pixels, smoothed with a Gaussian of σ=1.5 pixels. Radio contours are from a 5.13-GHz map made using data from *VLA* programme SJ0472 with a restoring beam of 0.48 arcsec × 0.28 arcsec, increasing by factors of 4 from 60 μJy beam^{-1}.

about 30 per cent of the data rejected to achieve good calibration and reliable maps. Mapping was further complicated by the presence of a bright source near the edge of the primary beam of the *VLA* antennas in the C band, but outside the primary beam at X band, and by inaccuracies in the bandpass calibration. Independent maps at lower and higher frequencies, and with suitably-chosen groups of reliable channels, resulted in excellent final maps centred at 5.13, 7.00, 9.00, and 10.7 GHz which were used independently, or combined, for spectral and structural analyses. Contours of the 5.13-GHz map, which has a noise of 9.1 μJy beam^{-1} with a synthesized beam of 0.48 arcsec × 0.28 arcsec, are shown in Figure 2.

We also made maps from the 1.4 and 5-GHz data for PKS J1421-0643 from archival *VLA* dataset AC755 (Cheung et al. 2008), taken on 2004 December 22. The *VLA* was in the A-array configuration for these observations for which about 26 and 10 min of data were taken at 1.4 and 5 GHz, respectively. Similar angular resolution (at 5 GHz) but poorer sensitivities were achieved from these earlier observations which also used 3C 286 as the primary flux-density calibrator.

2.3 *HST*

We observed PKS J1421-0643 with the WFC3/UVIS instrument on *HST* on 2018 February 22. The source was observed using the F555W (pivot wavelength 530.595 nm) and F814W (pivot wavelength 804.810 nm) filters (program GO-15376) in three and two separate dithered exposures totalling 1.35 and 0.98 ks, respectively. Source orientation was such that the jet direction extends between quasar diffraction spikes. We made final images for each filter using the pipeline-processed files corrected for charge transfer efficiency as input to the PYTHON DRIZZLEPAC TWEAKREG and ASTRODRIZZLE software routines, guided by the Space Telescope Science Institute (STScI) tutorials[4]. To correct for Galactic extinction the F814W and F555W flux densities have been increased by factors of 1.07 and 1.129, respectively, based on values from the NASA/IPAC Extragalactic Database (NED). Flux-density upper limits for undetected jet features are based on the mean and standard deviation of values found through placing the region of interest at multiple locations across the CCD, and are quoted at 3σ significance.

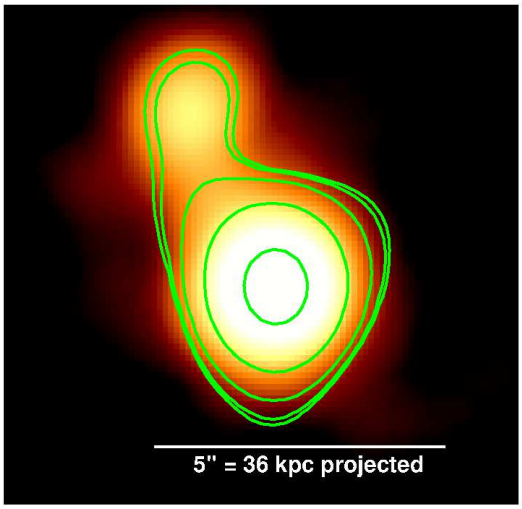

Figure 3. 0.5–5-keV *Chandra* image of PKS J1421-0643 in 0.0984-arcsec pixels, smoothed with a Gaussian of σ=5 pixels. Radio contours are from the 1.42-GHz map made using data from *VLA* programme AC755I with a restoring beam of 1.54 arcsec × 1.27 arcsec, logarithmically spaced between 3 and 200 mJy beam^{-1}.

3 JET RESULTS

3.1 Imaging

Figure 2 shows that *Chandra* detects a continuous jet extending NNE of the quasar core. After a bright knot that corresponds with 5-GHz radio emission the X-rays fade and the jet appears to kink slightly before a bright terminal region where the X-rays are brightest to the SE of a prominent 5-GHz knot. When compared with lower-resolution 1.4-GHz data, the X-ray and radio show good overall correspondence (Fig. 3).

For a quantitative investigation of the structure of the X-ray jet, starting from the reprocessed events file we first made azimuthal distributions of the counts in five radial bands (Fig. 4). The upper panel of this figure shows that PSF asymmetry may be preventing detection of the X-ray jet within 1 arcsec of the core. No excess counts are seen in the CCD readout direction, roughly orthogonal to the jet direction, proving that the 1/4-sub-array used for the observations was sufficient to mitigate any significant pile-up in the core emission. The lower panels show the jet position

[4] https://spacetelescope.github.io/notebooks/.

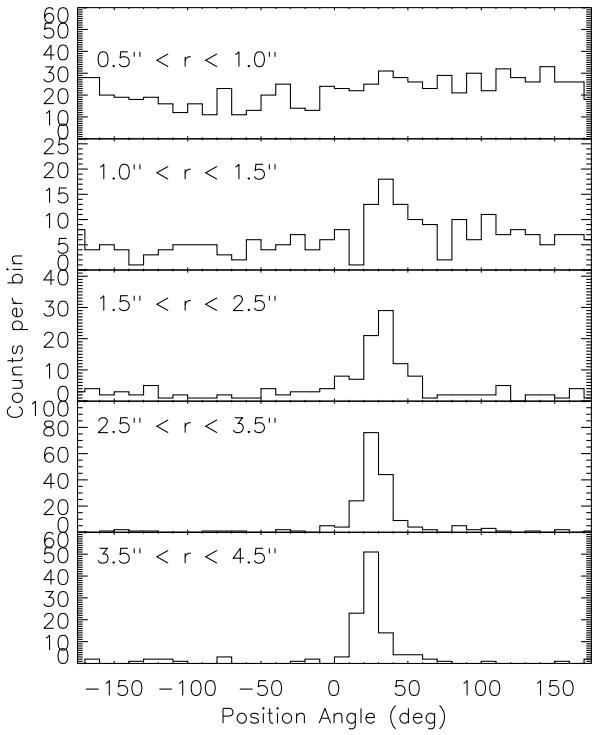

Figure 4. Azimuthal distributions of the source-centred 0.5–5-keV X-ray counts in five radial bands. No background is subtracted. Errors should be taken as Poissonian.

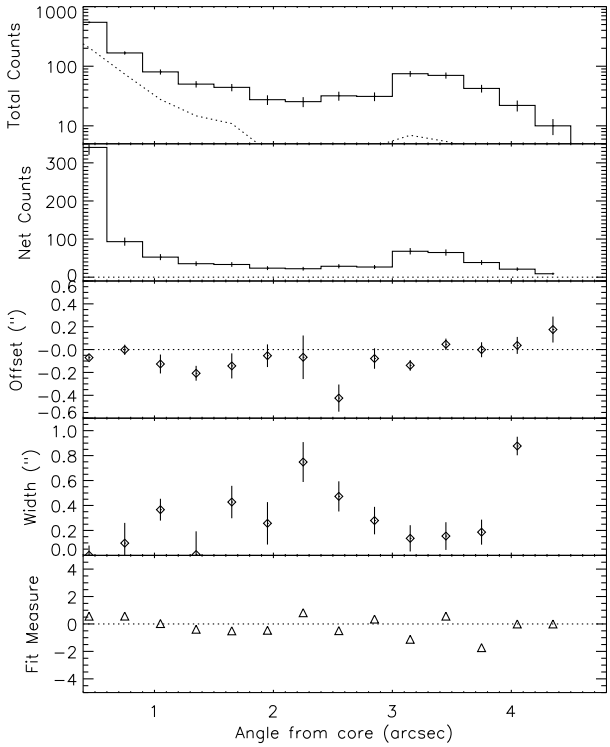

Figure 5. Fitted transverse structural parameters of the 0.5–5-keV X-ray jet measured in radial bins of length 0.3 arcsec. Panels from top to bottom show: 1. Total counts (histogram) compared with background from mirror-image counterjet direction (dashed line). 2. Net counts. 3. Offset from reference position angle of 25 degrees. 4. Excess width, defined as the sigma of the Gaussian needed to be added in quadrature to that of a point source in order to fit the data. 5. Fit measure, based on a Kolmogorov-Smirnov (K-S) test, with the K-S probability of achieving a better fit expressed in Gaussian standard deviation units, so that negative values correspond to better-than-average fits and positive values to worse-than-average fits.

angle shifting from between 30 and 40 degrees to between 20 and 30 degrees with increasing radial distance. We then placed a broad rectangle over the jet at a position angle of 25 degs (so centred on the jet where it is bright at about 3.7 arcsec from the core), and the rectangle's mirror-image in the counterjet direction to sample background. In radial bins of length 0.3-arcsec we have used a maximum-likelihood method to fit the centroid and width of the transverse profile of jet counts, with results shown in Figure 5. The middle panel quantifies the jet bending. Importantly, the panel below it finds the fainter parts of the jet in particular are detectably broadened, although emission at about 1.35 arcsec is unresolved in the transverse direction.

For further investigation of the structure of the X-ray jet we used the CIAO ARESTORE task to deconvolve the data and modelled PSF using the Richardson Lucy deconvolution algorithm. The provided documentation warns that the algorithm has a tendency to break faint continuous features into points, but it is nonetheless useful in our case (see Fig. 6) in confirming the direction of bending. The emission at 1.35 arcsec from the core, found in Figure 5 to be unresolved in the transverse direction, is confirmed from the analysis here to be dominated by a distinct knot at a position angle of 37° that is resolved along the jet but less resolved in the transverse direction.

Unlike the radio and X-ray, clear jet emission is not apparent in the optical (Fig. 7). From visual inspection, the most prominent feature close to the quasar is a diffuse source seen in the data at both frequencies about 3 arcsec to its NW.

3.2 Spectra

We have fitted X-ray spectra extracted from several regions shown in Figure 8. The large rectangular region samples the overall jet spectrum, excluding emission from the core, and chi-squared fitting finds those data fit well a single-component power law with no absorption in excess of Galactic: $\chi^2 = 16.3$ for 14 degrees of freedom (dof). The spectrum is shown in Figure 9. Assuming isotropic radiation, the jet's source-frame luminosity, corrected for Galactic absorption, is $3.2{\times}10^{45}$ erg s^{-1} (2–20) keV, but see the relativistic beaming discussion in Section 4.5.

Our sub-regions have been chosen with reference to the combined intensity in the X-ray and radio. They are defined as pie-slice segments of annular bands, and for computation of volume the symmetry axis is assumed to be the radius vector from the core that dissects the pie-slice into two equal parts. Jet region A incorporates the first radio and X-ray knot. In region B, despite a radio knot, the X-ray surface brightness drops. The final feature is divided into region C which includes the brighter X-ray part of the emission, and region D where a terminal radio feature corresponds to a drop in X-ray surface brightness, although the boundaries

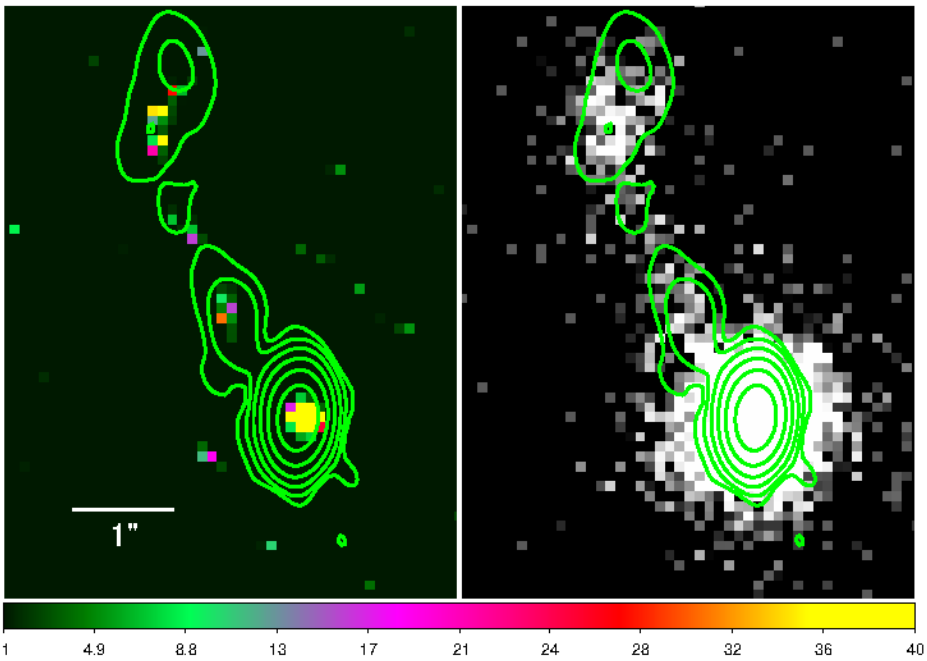

Figure 6. 0.5–5-keV *Chandra* images in 0.0984-arcsec pixels with radio contours from Fig. 2. **Left**: after PSF deconvolution showing the core and bent jet. The colour bar is linear in units of counts. The scale is chosen to show counts in features in the jet and the core is strongly saturated. **Right**: The unsmoothed data for reference.

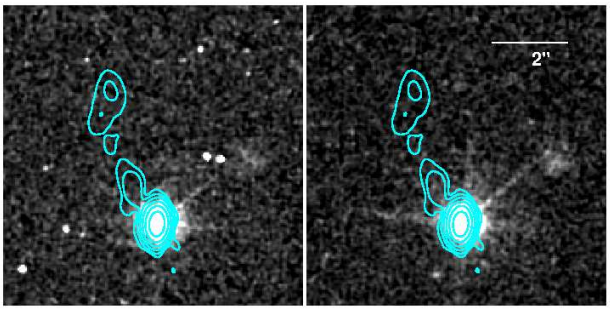

Figure 7. HST images (left F814W filter, right F555W filter) with radio contours from Fig. 2. The pixel size is 0.0395 arcsec and the images are smoothed with a Gaussian of σ=2 pixel. A diffuse source unrelated to the quasar is seen in both images about 3 arcsec to its NW, below the extension of the linear charge-transfer artefact that lies between the diffraction spikes.

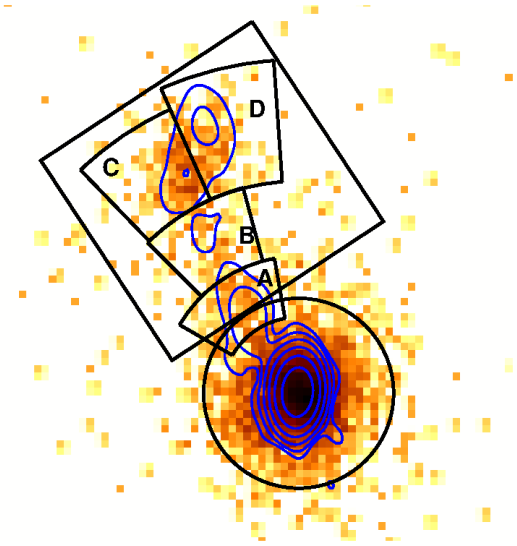

Figure 8. Unsmoothed X-ray data with radio contours of Fig. 2, showing regions used for data extraction.

are chosen to give similar numbers of net counts in regions C and D. This means that the impact of the lower X-ray-to-radio ratio at the extremity of the jet is not fully accommodated in our subsequent modelling. The annulus is completed, with jet region excluded, to sample the background for each extraction, resulting in the best possible exclusion of (weak) contributions from the wings of the quasar point spread function (PSF). We note that there is necessarily some blending of jet features due to the PSF. Spectral results are given in Table 3, where it can be seen that X-ray spectral index is found to be constant down the jet, within uncertainties.

The radio and optical flux densities for the jet regions are given in Table 4. Tables 3 and 4 also include values for the quasar nucleus which is discussed further in Section 5. The jet radio flux densities correspond to unexpectedly steep spectra in all regions, while the core gives a typical flat spectrum ($\alpha_r \approx 0.4$) characteristic of partial self-absorption. The radio jet spectra are steeper even than expected for synchrotron-emitting electrons above the energy-loss break in a continuous injection model. Indeed, the spectral shapes, which for regions B, C, and D show clear steepening with increasing frequency within the measured band (Table 4),

Table 3. X-ray power-law spectral fits.

(1) Region	(2) Net counts (0.5-10 keV)	(3) α_x	(4) 1-keV normalization (nJy)	(5) $N_{H_{int}}$ (10^{22} cm^{-2})	(6) χ^2/dof
Core	2748	0.78 ± 0.10	$40.5^{+4.8}_{-4.1}$	$6.7^{+3.4}_{-2.9}$	95.4/105
Jet	339	0.70 ± 0.20	4.1 ± 0.6	—	16.3/14
...	...	0.65 ± 0.19	4.2 ± 0.6	—	18.6/14*
Jet A	38	0.53 ± 0.86	$0.46^{+0.33}_{-0.26}$	—	25.5/29*
Jet B	51	0.27 ± 0.50	$0.50^{+0.23}_{-0.18}$	—	44.5/47*
Jet C	103	0.62 ± 0.35	$1.23^{+0.33}_{-0.28}$	—	83.6/80*
Jet D	96	0.70 ± 0.35	$1.22^{+0.34}_{-0.29}$	—	87.7/70*

(3), (4) and (5) Uncertainties are 90% for 1 interesting parameter. (6) χ^2 goodness of fit unless *, for which the wstat statistic associated with cstat is given.

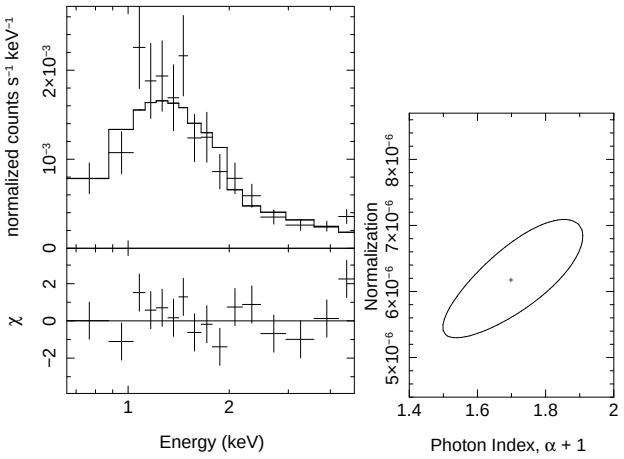

Figure 9. Left: X-ray spectrum of the jet fitted to a power law with no absorption in excess of the Galactic value (Table 3). Right: Uncertainty contour in spectral index and 1 keV-normalization (photons cm^{-2} s^{-1} keV^{-1}) shown at the level of 90% confidence for one interesting parameter.

match emission from within the synchrotron exponential tail of an electron spectrum with a maximum cut-off energy, as shown in our modelling below.

A comparison of the archival (2004) 1.4-GHz and our new (2018) 5.13-GHz data gives a spectral index of 1.3 ± 0.1 for that part of the jet that can be cleanly separated from the core at the resolution of the 1.4-GHz data. This shows that the spectrum of the jet continues to flatten to lower radio frequencies in the manner modelled in Section 4.3.

4 JET MODELLING AND DISCUSSION

4.1 Radio synchrotron emission and detection of γ_{max}

We have modelled the synchrotron emission following Hardcastle, Birkinshaw & Worrall (1998), where the electron spectrum extends between Lorentz factors γ_{min}, for which we adopt a value of 10, and γ_{max}. The value of γ_{max} is unimportant to the production of X-ray iC radiation, and is normally taken to be any value higher than that needed to produce the observed radio synchrotron emission and any emission at higher frequencies that is consistent with a power-law extension. However, in PKS J1421-0643, a match to the exponentially falling level of radio emission gives a measurement of γ_{max} that depends only on intrinsic magnetic field strength, B (see Section 4.3).

The measured value of B depends on relativistic beaming and how close the radio source is to being at minimum energy. After passing through terminal hotspots, jet plasma no longer has bulk relativistic motion and forms lobes seen at highest contrast to the jets for sources whose jets are in the plane of the sky, i.e., radio galaxies. X-ray lobe iC detections in powerful radio galaxies find magnetic fields that are within a factor of a few of minimum energy for no proton contribution (Croston et al. 2005), lending support to the same state of play in their kpc-scale jets. We therefore adopt minimum energy ($B = B_{me}$), noting that this has been the common assumption in modelling kpc-scale quasar emission although sometimes assuming equal energy density in protons and electrons (e.g., Schwartz et al. 2006), which would increase B_{me} by the small factor of $2^{(1+\alpha)/3}$ for synchrotron emission of spectral index α (in our case $\alpha = 0.65$, see below). An alternative common choice is to use equipartition magnetic field strengths, B_{eq}, and we note that

$$B_{eq} = B_{me}\sqrt{(3+\alpha)/2(1+\alpha)}. \quad (1)$$

4.2 Modelling rationale

In modelling PKS J1421-0643 we are strongly influenced by its high redshift. The energy density of the CMB, which increases as $(1+z)^4$, is thus likely to dominate that of the magnetic field. Written in SI units[5], the CMB energy density is the larger of the two if

$$B < 0.32\ \Gamma\ (1+z)^2 \quad \text{nT}, \quad (2)$$

where Γ is the bulk Lorentz factor of the jet. Even for $\Gamma \approx 1$, at $z = 3.689$ any jet magnetic field less than 7 nT would cause iC losses on the CMB to dominate synchrotron losses.

[5] 1 nT = 10 μG

Table 4. Radio and optical flux densities, S, and volumes for the extraction regions.

(1) Region	(2) S(5.13 GHz) (mJy)	(3) S(7.00 GHz) (mJy)	(4) S(9.00 GHz) (mJy)	(5) S(10.68 GHz) (mJy)	(6) α_{r_1}	(7) α_{r_2}	(8) $S(3.73\times10^{14}$ Hz) (μJy)	(9) $S(5.65\times10^{14}$ Hz) (μJy)	(10) Volume (arcsec^3)
Core	237.5 ± 1.4	217.4 ± 1.0	193.3 ± 0.4	180.9 ± 0.7	0.28 ± 0.02	0.44 ± 0.01	134 ± 3	82 ± 3	–
Jet A	1.21 ± 0.01	0.71 ± 0.01	0.46 ± 0.01	0.30 ± 0.02	1.72 ± 0.05	1.7 ± 0.1	< 0.39	< 0.37	0.95
Jet B	0.25 ± 0.02	0.11 ± 0.01	0.01 ± 0.02	0.02 ± 0.02	2.6 ± 0.4	4.0 ± 2.4	< 0.48	< 0.24	1.15
Jet C	0.39 ± 0.02	0.26 ± 0.01	0.07 ± 0.02	0.01 ± 0.02	1.3 ± 0.2	5.2 ± 1.1	< 0.33	< 0.13	1.49
Jet D	0.92 ± 0.02	0.50 ± 0.01	0.24 ± 0.02	0.08 ± 0.02	1.9 ± 0.1	2.9 ± 0.3	< 0.67	< 0.24	2.01

Uncertainties are 1σ. Upper limits are 3σ. (6) α_{r_1} is two-point radio spectral index 5.13 to 7 GHz. (7) α_{r_2} is two-point radio spectral index 7 GHz to either 9 or 10.68 GHz as chosen to give the smaller uncertainty.

The factor by which the iC losses are faster than those to synchrotron for a given electron is given by the ratio of energy density in the CMB, $u_{\rm CMB}$, to that in the magnetic field, $u_{\rm B}$. For B in units of nT,

$$u_{\rm CMB}/u_{\rm B} \approx 0.1\ \Gamma^2\ (1+z)^4/B^2. \quad (3)$$

Intrinsic minimum-energy magnetic fields of quasar kpc-scale jets are difficult to measure because of uncertain relativistic beaming. For low-redshift quasar samples, values of a few to 10 nT are inferred (e.g., Hogan et al. 2011; Marshall et al. 2018). However, to model the beaming such results assume that the X-ray emission in quasars at low redshift is of iC origin, something now proved to be unlikely in general by optical polarization measurements and gamma-ray upper limits for several objects (e.g., Cara et al. 2013; Meyer & Georganopoulos 2014; Meyer et al. 2015; Breiding et al. 2017). In bright kpc-scale jet knots of nearby powerful radio galaxies where X-rays are detected and beaming is small and constrained by structural measurements more reliably than for quasars, estimates from synchrotron modelling typically find values of $B_{\rm me}$ between 10 and 30 nT (e.g., Worrall & Birkinshaw 2005; Kataoka et al. 2008; Worrall et al. 2012). Unlike most quasars included in Figure 1, PKS J1421-0643 is at a redshift where the relativistic electrons are expected to lose more of their energy via iC scattering on the CMB (iC-CMB) than via synchrotron radiation, even for modest values of Γ,

The measured jet X-ray spectrum of PKS J1421-0643, of $\alpha_{\rm x} \approx 0.65$, is an excellent match to that expected from synchrotron or iC radiation from an electron spectrum that has undergone particle acceleration and not suffered significant energy losses (e.g., Achterberg et al. 2001). Energy losses would be manifest as a steepening of the spectrum to higher energies by a value of $\Delta\alpha \approx 0.5$ (or somewhat larger). Such a break is commonly observed at rest frequencies between 10^{12} and 10^{15} Hz in the kpc-scale jet knots of nearby radio galaxies with detections spanning the radio and X-ray energy bands (e.g., Böhringer et al. 2001; Hardcastle, Birkinshaw & Worrall 2001), including jets of higher power and so more comparable to quasars (e.g., Worrall & Birkinshaw 2005; Worrall et al. 2012). The energy-loss time implied by the location of the spectral break often roughly matches the light travel time across the knots, and so particle acceleration is not required to occur throughout the knots (consistent with arguments made for Pictor-A based on short-timescale X-ray variability: Marshall et al. 2010; Hardcastle et al. 2016), and the X-rays are undoubtedly of synchrotron origin in such sources. Similar spectral breaks are seen in a number of low-redshift quasars, although the spectra do not extrapolate to fit the X-ray data (e.g., Sambruna et al. 2006; Godfrey et al. 2012; Breiding et al. 2017; Meyer et al. 2017). In the high-redshift quasar PKS J1421-0643 it appears that acceleration processes are not raising electrons to high enough energy for the spectrum to reveal a signature of energy losses or for X-ray synchrotron emission to be achieved, and the high redshift provides good reason to adopt an iC explanation for the X-ray emission. It is further notable that the X-rays fade after the sharp radio bend towards the end of the jet, consistent with an iC-CMB interpretation for which the X-ray to radio ratio is more strongly dependent on angle to the line of sight than alternative synchrotron explanations.

4.3 Modelling results

We have modelled the electron spectrum as extending from $\gamma_{\rm min} = 10$ to $\gamma_{\rm max}$ as $\propto \gamma^{-2.3}$ so as to produce synchrotron emission of spectral index $\alpha = 0.65$ at radio frequencies below our observations, and such that the X-rays match the spectrum expected from iC scattering of the CMB. We used equations in the form given by Worrall (2009) to model the X-rays via the iC-CMB process. An illustrative example of the data and spectral model for the Jet-D region is shown in Figure 10.

Angle to the line of sight, θ, and bulk Lorentz factor, Γ, give the Doppler factor, δ. Rather than assume $\delta = \Gamma$, as has often been the case in quasar jet modelling (e.g., Schwartz et al. 2006), here we explore all reasonable values of Γ and θ that give the observed level of X-ray emission, treating each region as a separate spherically-emitting volume. Results are shown in Figure 11, where shaded regions indicate fits within the X-ray normalization uncertainties of Table 3. The *a priori* probability of the approaching jet having a line-of-sight angle between θ and $\theta + \Delta\theta$ is $\sin\theta\Delta\theta$, and so large values of θ are preferred, consistent with $\delta = \Gamma$. This suggests that Γ is likely to have a value of a few, at most. The angle to line of sight is consistent with the range of values expected for quasars, without needing to be of the very small value often assumed true of a blazar.

In Table 5 we give parameter values where $\Gamma = 4$ is adopted for all jet regions, under the hypothesis that the jet does not suffer significant bulk deceleration. The uncertainties given for magnetic field strength in Table 5 are not constrained in this way, and they apply to all allowed com-

Table 5. Values for physical parameters, constrained to $\Gamma = 4$ except in the case of B.

(1) Region	(2) r(arcsec)	(3) $\gamma_{\rm max}$	(4) Γ	(5) θ (deg)	(6) δ	(7) $\log_{10}(\tau_{\rm r})$ (yr)	(8) $\log_{10}(\tau_{\rm x})$ (yr)	(9) $\nu_{\rm r}$ (MHz)	(10) B (nT)	(11) $P_{\rm jet}(10^{46}$ erg s$^{-1})$
Jet A	0.61	7200	4	15.3	3.8	4.6	6.0	1.6	$3.09^{+1.1}_{-0.39}$	3.0
Jet B	0.65	5000	4	14.8	3.9	4.8	6.0	1.5	$2.66^{+0.57}_{-0.27}$	2.5
Jet C	0.71	5000	4	12.3	4.6	4.8	6.0	1.0	$2.31^{+0.26}_{-0.16}$	2.3
Jet D	0.78	5000	4	14.5	4.0	4.8	6.0	1.7	$2.95^{+0.39}_{-0.2}$	4.5

(1) Region from Fig. 8. (2) Angular radius of the equivalent spherical emitting region. (3) Maximum value of the electron Lorentz factor, as constrained by the steep radio spectra. (4) Value of jet Lorentz factor. (5) Angle to line of sight. (6) Doppler factor. (7) Logarithm of lifetime of radio-emitting electrons of $\gamma_{\rm max}$. (8) Logarithm of lifetime of electrons emitting iC-CMB in the X-ray at 1 keV. (9) Frequency at which 1-keV-emitting electrons produce radio-synchrotron emission, in units of MHz. (10) Intrinsic magnetic field strength with uncertainties that take into account the uncertainties in beaming parameters shown in Fig. 11, and so are not constrained to $\Gamma = 4$. (11) Jet power for $\Gamma = 4$ and cyclindrical section of radius given in column 2.

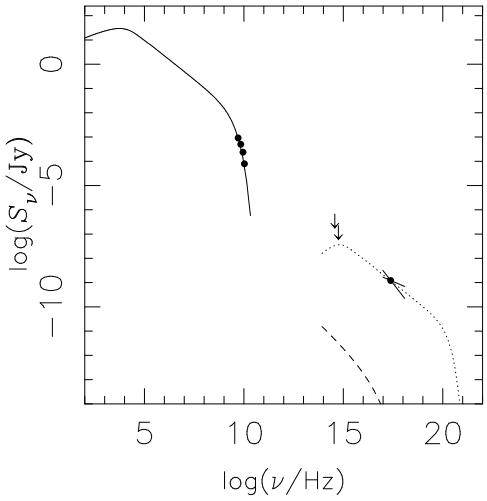

Figure 10. Spectrum of region Jet D. Measurement detections and upper limits are from Tables 3 and 4. Continuous line shows synchrotron emission from an electron spectrum modelled as described in the text, with the radio data falling on the high-energy exponential tail. The dotted line is iC-CMB modelled to give the X-ray emission, using parameters from Table 5, and the dashed line is the synchrotron self-Compton prediction. Plots for jet regions A, B, and C are similar in their key features (Fig. A1).

binations of Γ and θ from Figure 11. It is immediately clear that for PKS J1421-0643 the condition in Equation (2) is satisfied, and from Equation (3) the electron losses to iC scattering on the CMB are much faster (by a factor > 80) than those to synchrotron losses, including, of course, for those electrons responsible for the synchrotron radiation observed in the radio band.

With regards the dominance of iC losses we should mention an additional uncertainty, which is jet volume. In Section 3.1 we found that in general the jet is resolved in width. From Figure 5 we find that the median transverse width over the jet length incorporating regions A to D has a Gaussian σ of 0.27 arcsec, for which the radius of an equivalent cylinder is 0.54 arcsec. This is on average about 20 per cent smaller than the radii used in Table 5. However, scaling with volume is relatively weak. For example, if the volume of jet region A is reduced by a factor of four the black shaded region in Figure 11 (left panel) moves a little to the left and up, to slightly larger values of δ. The value of B then increases slightly from $3.1^{+1.1}_{-0.4}$ to $4.8^{+1.5}_{-0.6}$ nT, but not enough to affect the conclusion of iC dominance.

The combination of the steeply falling radio spectrum and iC-CMB interpretation which requires only a single electron population, means that the jet should be largely invisible in the sub-mm to mid-infrared band and in high-energy gamma-rays (Fig. 10).

4.4 Particle lifetimes

In Table 5 we give values for the lifetimes of electrons, using $\Gamma = 4$ as the example. For the jet plasma to reach region D it must travel a deprojected distance of about 130 kpc, taking roughly 4×10^5 yr which is about six times longer than the radiative lifetime of the electrons of $\gamma_{\rm max}$ producing the radio. This argues for a number of regions of particle re-acceleration along the jet, presumably related to the observed non-uniform radio intensity and deviations from a straight path. For iC losses dominating over synchrotron, as here, the lifetime of electrons of Lorentz factor γ can be written simply as

$$\tau \approx 2.3 \times 10^{12} \Gamma^{-2} \gamma^{-1} (1+z)^{-4} \quad \text{yr}. \qquad (4)$$

An increase in τ by a factor of six would require $\Gamma \approx 1.6$ which Figure 11 shows to be inconsistent with data for region C, and other regions would then prefer smaller θ and so a longer jet. Values of $\Gamma > 4$ would require a larger number of re-acceleration regions. It is unlikely that the requirement for re-acceleration along the jet can be removed. It is satisfying that the granularity in radio structure suggested by our $\Gamma = 4$ solution is roughly consistent with the radio observations, although it should be noted that the radio appearance is strongly driven by radio beam size.

There is no requirement for re-acceleration along the jet for the lower-energy X-ray-emitting electrons, and were jet fuelling to cease we might expect eventually to detect this jet in the X-ray but not the radio, before its ultimate disappearance. We would first expect the radio-loudness of the core to have diminished considerably.

An expectation from the lifetime of the X-ray-emitting electrons being longer than the jet travel distance is that the X-ray surface brightness should be smooth.

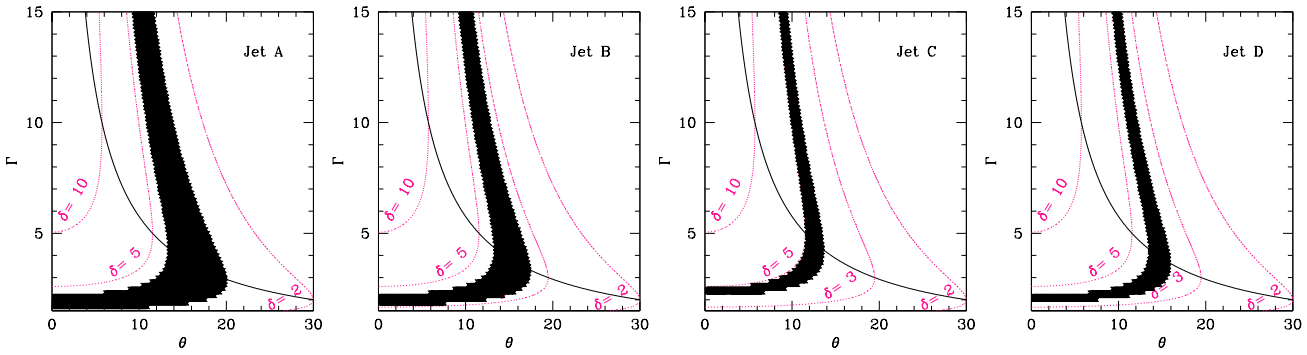

Figure 11. Lorentz factor and angle to line of sight for model fits to jet regions A to D. The shaded areas show allowed values of Γ and θ within uncertainties on the X-ray measurements. Dotted lines show contours of Doppler factor, δ, and solid curves are the locus of $\delta = \Gamma$.

Tavecchio, Ghisellini, & Celotti (2003) highlighted the relatively strong correspondence of X-ray and radio knots in some low-redshift quasar jets as a problem for the iC-CMB model and sought solutions in terms of clumping and adiabatic losses. In contrast, in PKS J1421-0643 the X-ray profile is flat beyond the core and out to 3 arcsec where there is brightening and sharp bending (Fig. 5), consistent with a long-lived electron population being responsible for the X-ray emission. However, as the deconvolution (Fig. 6) suggests a degree of knottiness over this length, deeper data would be required to draw reliable conclusions. The range of surface brightness when the terminal region is included is a factor of roughly three which is less than the factor greater than 10 typical of low-redshift quasar X-ray jets such as in 3C 273 (Sambruna et al. 2001; Marshall et al. 2001) and PKS 0637-752 (Schwartz et al. 2000; Chartas et al. 2000) and closer to expectations for the iC-CMB model. We note that PKS J1421-0643 is significantly shorter in angular extent and presents fewer resolution elements than the low-redshift jets for which more-detailed multiwavelength comparisons are possible.

4.5 Jet power

For a tangled minimum-energy magnetic field of energy density $u_{\rm B_{me}}$, where minimum energy is calculated with respect to all particles and the field, we can re-cast equation B17 of Schwartz et al. (2006) to give jet power, for $\alpha \neq 0.5$, as

$$P_{\rm jet} \approx \frac{\Gamma^2 \beta c A u_{\rm B_{me}}}{(1+\alpha)} \left[\frac{4(3+\alpha)}{3} + \frac{(\Gamma-1)}{\gamma_{\rm min}\Gamma} \frac{(1+k_2)}{(1+k_1)} \left(\frac{2\alpha-1}{2\alpha} \right) \left[\frac{1-(\gamma_{\rm max}/\gamma_{\rm min})^{-2\alpha}}{1-(\gamma_{\rm max}/\gamma_{\rm min})^{-(2\alpha-1)}} \right] \right]. \quad (5)$$

Here βc is jet velocity ($\beta = \sqrt{1-\Gamma^{-2}}$), A is the cross-sectional area of the jet, $\alpha, \gamma_{\rm min}, \gamma_{\rm max}$ are the spectral parameters of the synchrotron-emitting component as defined in Section 4.1, k_1 is the ratio of the energy density of other particles to that of the synchrotron-radiation emitting electrons/positrons, and k_2 is the ratio of rest-mass energy of other particles to that in electrons/positrons.

Our calculations in Table 5 are for an electron–positron jet, with $k_1 = k_2 = 0$, for reasons given in Section 4.1 (and see fuller discussion in Sikora, Nalewajko & Madejski 2020). The average $P_{\rm jet}$ for the four regions is roughly 3×10^{46} erg s^{-1}, and the spread of values (Table 5) is indicative of systematic uncertainties given the choice of beaming parameters.

The jet power we have found is small in comparison with the quasar luminosity of about 4×10^{47} erg s^{-1} (Section 5), and we consider if it might be underestimated. A simple way of allowing a larger value of $P_{\rm jet}$ is to select larger Γ consistent with Figure 5. Very large Γ would make PKS J1421-0643 highly special, and so we adopt Γ = 10 as a likely upper bound, giving a new average upper bound over the four regions of $P_{\rm jet} \approx 2 \times 10^{47}$ erg s^{-1}.

The other potential contributor to higher jet power would be heavy particles in the jet. In Equation 5, the first term represents the rate of advection of internal energy (particles and magnetic field), and is largely independent of particle composition, except through a small positive increase of $u_{\rm B_{me}}$ with increasing k_1. The second term, which represents the contribution due to the ram pressure of the particles, is negligible compared with the first term in the case of an electron–positron jet, but becomes dominant with the insertion of heavy particles due to the increase in k_2.

An extreme case is to allow charge neutrality by pairing electrons with positive ions. If the positively-charged material has cosmic abundances, then $k_2 \approx 2200$ (Schwartz et al. 2006). The result for $P_{\rm jet}$ then depends on how energetically important the positive ions are compared with the electrons, and the smaller the value of k_1 the larger the contribution to $P_{\rm jet}$ (the weak positive dependence of $u_{\rm B_{me}}$ on k_1 is more than offset by the $(1+k_1)^{-1}$ factor). Were charge neutrality preserved using a proton spectrum of shape similar to that of the electrons, the minimum Lorentz factor of the protons would be k_1/k_2 that of the electrons, which is a situation that is violated for low k_1 and the low value of electron $\gamma_{\rm min}$ needed for a iC-CMB model to explain X-ray emission. Thus, to allow both charge neutrality and a low k_1 (a value $k_1 = 1$ is used, for example, by Schwartz et al. 2006) the proton spectrum must either be much flatter than that of the electrons, and not easily matched to particle acceleration models, or the proton spectrum must turn up rapidly at low energies such that most of the jet protons are cold. Although we consider charge neutrality provided by positive ions to be unlikely, in the situation of $k_1 = 1, k_2 = 2200$,

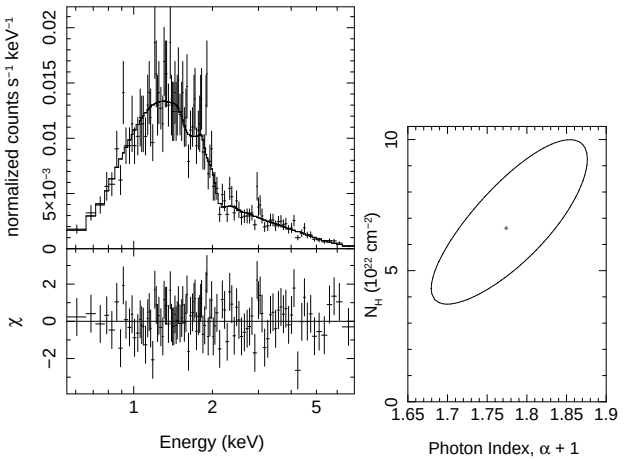

Figure 12. Left: X-ray spectrum of the core fitted to a power law and requiring additional absorption at the redshift of PKS J1421-0643 (Table 3). Right: Uncertainty contour in spectral index and intrinsic $N_{\rm H}$ shown at the level of 90% confidence for one interesting parameter.

we find for PKS J1421-0643 that $P_{\rm jet} \approx 2 \times 10^{47}$ erg s^{-1} for $\Gamma = 4$, and it would reach about 10^{48} erg s^{-1} for $\Gamma = 10$. These last two jet powers increase by a factor of roughly two if minimum-energy is between only the electrons and field despite the presence of heavy particles (a disappearance of the $(1 + k_1)^{-1}$ term on the right hand side of Equation 5 dominates that result).

Our discussion has shown that quasar jet power is uncertain. In what we consider to be the most likely situation of an electron–positron jet, and adopting $\Gamma \approx 4$, the power is about 3×10^{46} erg s^{-1}. It could potentially reach 10^{48} erg s^{-1} in the extreme situation of the jet being very fast, gaining charge neutrality from positive ions, and minimum energy applying between the light particles and magnetic field alone, but jet power would then exceed estimates of the quasar bolometric luminosity.

In Section 3.2 we found the 2–20 keV X-ray luminosity of the jet to be 3.2×10^{45} erg s^{-1}, under isotropic assumptions, giving a modelled bolometric luminosity between observed frequencies of 10^{15} and 10^{20} Hz (see Figures 10 and A1) a factor of nine larger. For iC-CMB emission we must take into account the beaming pattern, which causes a correction of $\delta^{-(4+2\alpha)}$ (Dermer 1995). This corrects the isotropic X-ray luminosity to be about 2×10^{42} erg s^{-1} and the bolometric jet luminosity to be $L_{\rm bol-jet} \approx 2 \times 10^{43}$ erg s^{-1}. This is only 0.07 per cent of the jet power of $P_{\rm jet} \approx 3 \times 10^{46}$ erg s^{-1} for an electron–positron jet. The radiated fraction is smaller if the jet contains heavy particles. Essentially all the jet power is therefore available for heating ambient gas.

5 THE QUASAR CORE

The X-ray spectrum of the core gives a good fit to a single-component power law but there is relatively high absorption in excess of the Galactic value (Figure 12). Visual comparison between the shape of the jet spectrum (Figure 9) and that of the core (Figure 12) shows it is indeed in their relative levels of low-energy emission where they differ.

When the excess absorption is placed as intrinsic to the source, the column density is $6.7^{+3.4}_{-2.9} \times 10^{22}$ cm^{-2}. The spectral index, $\alpha_{\rm x} = 0.78 \pm 0.10$, for this high-redshift source does not follow the trend hinted at in Marshall et al. (2018) of core spectral indices becoming flatter with increasing redshift. Details of the spectral fit are given in Table 3. The source-frame luminosity, corrected for absorption, is 3.0×10^{46} erg s^{-1} (2–20 keV).

The redshift of the excess absorption is not constrained by the data, with any redshift between 0 and 4 lying within 90% confidence bounds. We could find no reported evidence of absorption in our Galaxy in this relatively high-Galactic-latitude direction that would not be taken into account by the Galactic value, for example molecular gas, and it would be highly unusual for that gas to have a lot of structure on a scale of a few arcsec, so as to affect the core and not the jet. (Formally we can set a 90 per cent upper limit of excess absorption $N_{\rm H} < 2.6 \times 10^{21}$ cm^{-2} at $z = 0$ in front of the jet.) Although it is notable that the quasar is associated with a damped Lyα (DLA) system at $z = 3.449$, the DLA profile suggests $N_{\rm H\,I} = 2.5 \times 10^{20}$ cm^{-2} (Ellison et al. 2001). While Bechtold et al. (2001) have detected X-ray absorption of order 10^{21} cm^{-2} potentially due to a DLA system for one quasar, for PKS J1421-0643 absorption attributable to the DLA is significantly lower than the X-ray absorption we find. So, the X-ray absorption of $\approx 7 \times 10^{22}$ cm^{-2} is likely to be intrinsic to the quasar. Ellison et al. (2005) note a DLA- and X-ray-derived discrepancy for another quasar, B038-436 at $z = 2.863$ (DLA at $z = 2.347$), pointing out that dustless gas near the quasar or an extinction curve significantly different from that of our Galaxy or the Small Magellanic Cloud might be responsible. The discrepancy is of similar size for PKS J1421-0643, and the same explanations may apply. Such high intrinsic absorption is unexpected from simple unification schemes (e.g., Barthel 1989).

Indeed, it has been known for decades that the cores of radio-loud quasars, can, but do not always, show evidence of excess intrinsic absorption, and it has been claimed that the level of that absorption increases with increasing redshift (e.g., Elvis et al. 1994a; Reeves & Turner 2000; Page et al. 2005). There are known systematic effects in the sense that absorption shows up first at the lowest X-ray energies, and so for a fixed observing band the absorption must be larger for detection in higher-redshift sources, complicating statistical inference related to redshift trends. While it has been suggested that intrinsic spectral curvature might instead be responsible for appearing as excess absorption (e.g., Tavecchio et al. 2007b), and deciphering the correct model is difficult (Ben Haim, Behar & Mushotzky 2019), most authors favour absorption along the line of sight, possibly associated with a warm-hot intergalactic medium (e.g., Eitan & Behar 2013; Arcodia et al. 2018). Where absorption is detected in high-redshift sources it has tended to be at levels of a few times 10^{22} cm^{-2} (Yuan et al. 2006), and this is true for PKS J1421-0643. We summarize properties for the high-redshift quasars with resolved X-ray jets from Table 1 in Table 6, where it can be seen in column (3) that three of the five have such levels of intrinsic absorption, while two do not.

Our *HST* data give quasar flux densities of 134 ± 3 and 82 ± 3 μJy at 3.725×10^{14} and 5.65×10^{14} Hz, respectively, confirming the level of redness reported by Ellison et al.

Table 6. Core and jet properties of quasars at $z > 3.5$ with X-ray jets, listed in order of increasing z.

(1) Name	(2) $L_{\rm core_X}$ (2–10 keV) 10^{46} erg s^{-1}	(3) $N_{\rm H_{core(int)}}$ 10^{22} cm^{-2}	(4) $\alpha_{\rm core_X}$	(5) $L_{\rm jet_X}$ (2–10 keV) 10^{45} erg s^{-1}	(6) $L_{\rm jet_X}/L_{\rm core_X}$ %	(7) $\alpha_{\rm jet_r}$	(8) $\alpha_{\rm jet_X}$	(9) Jet $\nu_X S_X/\nu_r S_r$	(10) Ref.
PMN J2219-279	1.8	< 0.6	0.34 ± 0.06	0.4	2	...	...	...	1
PKS J1421-0643	2.0	$6.7^{+3.4}_{-2.9}$	0.78 ± 0.1	2.1	10	Table 4	0.65 ± 0.19	71	2
4C+62.29	5.7	$2.35^{+0.78}_{-0.71}$	$0.74^{+0.08}_{-0.14}$	4.2	7	0.93 ± 0.09	$0.62^{+0.16}_{-0.17}$	22	3
GB 1508+5714	2.8	< 0.33	0.52 ± 0.04	0.7	2.5	1.4 ± 0.2	$0.83^{+0.15}_{-0.14}$	158	4, 5, 6, 7
GB 1428+4217	40	$2.32^{+1.29}_{-1.26}$	0.44 ± 0.04	1.3	0.3	1.0 ± 0.1	$0.64^{+0.39}_{-0.38}$	205	6, 7

(2) Core unabsorbed rest-frame X-ray luminosity; (3) Core X-ray intrinsic column density; (4) Core X-ray spectral index; (5) Jet isotropic rest-frame X-ray luminosity; (6) Jet/core X-ray ratio, where both treated as isotropic; (7) Jet radio spectral index, where available; (8) Jet X-ray spectral index, where available; (9) Jet X-ray to radio ratio, where available, using flux densities at 1 keV and 5 or 1.4 GHz; (10) References: 1. Saez et al. (2011); 2. This work; 3. Cheung et al. (2006) 4. Siemiginowska et al. (2003b) 5. Yuan et al. (2006) 6. McKeough et al. (2016) 7. Cheung et al. (2012)

(2005). Even the lower-frequency band is sampling emission from a rest-frame wavelength less than 250 nm for which the spectral-energy-distribution fitting of Elvis et al. (1994b) for lower-redshift quasars gives an average bolometric correction of roughly a factor of six. If we are to apply this to PKS J1421-0643 we find a bolometric quasar luminosity of $L_{\rm bol} \approx 4 \times 10^{47}$ erg s^{-1}, and using the expression in Schwartz et al. (2006) the energy density of quasar emission exceeds that of the CMB only within about 13 kpc from the core, or one tenth the distance down the jet based on modelling in Table 5. We are thus justified in ignoring this additional radiation field in Section 4.3.

The X-ray results are heavily dominated by the longer 2018 data (see Table 2 for dates). In order to search for possible variability between 2007 and 2018 we must use model-fitted results because of changes in the *Chandra* response, and we have fitted the power-law model with intrinsic absorption separately to the data from the two epochs. The (poorly constrained) absorption measured from 2007 is consistent within errors with that from 2018, but the normalization indicates significant brightening (by a factor of about two) over the eleven-year interval (Fig. 13). Within the 2018 observing period it suffices to examine count rates, and no day-to-day variations are measured over the five days of observation. The long-term variability translates into an upper limit on source size of about $11/(1+z)$ light years, or roughly 0.7 pc.

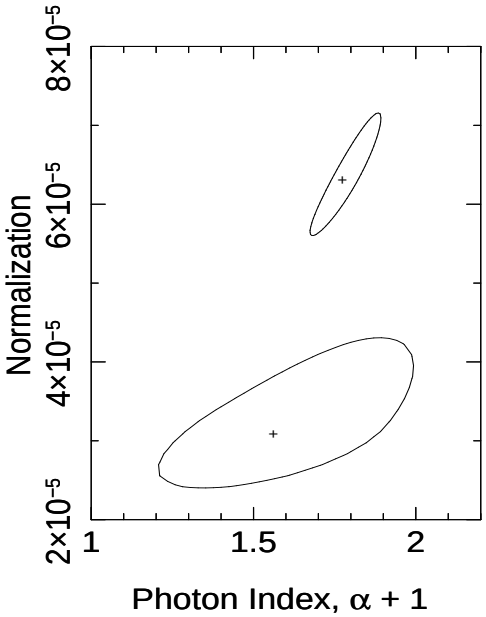

Figure 13. Uncertainty contours (90% confidence for one interesting parameter) in spectral index and 1 keV-normalization (photons cm^{-2} s^{-1} keV^{-1}) for the core emission from data taken in 2018 (upper contour) and the archival data from 2007 (lower contour). The results show variability of about a factor of two over eleven years.

6 HIGH-Z QUASARS WITH RESOLVED X-RAY JETS

Table 6 compiles interesting core and jet properties of PKS J1421-0643 alongside those of the four other quasars at $z > 3.5$ with resolved X-ray jets listed in Table 1. We see from the core emission that they are all relatively X-ray-luminous quasars. In contrast, out of a sample of 15 quasars at $z > 4.5$ selected by compact steep-spectrum radio emission, only two have rest-frame 2–10 keV luminosity more than 10^{46} erg s^{-1} (Snios et al. 2020). An uncertain but significant fraction of the unresolved X-ray emission in the X-ray-jetted quasars is likely to be beamed and related to pc-scale jet emission, contributing to enhanced luminosity and the relative flatness of the X-ray spectrum, as historically argued for lower-redshift samples (Zamorani et al. 1981; Worrall et al. 1987; Wilkes & Elvis 1987) and more recently studied at high redshift (e.g., Bassett et al. 2004; Wu et al. 2013). Given that variability has set an upper limit to the size of the nuclear X-ray emission region of about 0.7 pc in PKS J1421-0643, a radio study using Very Long Baseline Interferometry would be a crucial to modelling that could estimate if the fraction of core X-ray emission attributable to a (misaligned) blazar-type jet is significant in this quasar.

The jet luminosities in Table 6 are calculated assuming the X-ray emission is isotropic, but this is highly unlikely

to be the case whatever the true emission mechanism. In Section 4.5 we comment on the strong correction if indeed an iC-CMB explanation holds. The (isotropic) jet-to-core ratio (column 6) does however give a value that can be easily compared between sources. We note that the value of 10 per cent for PKS J1421-0643 is high, which may be related to some combination of favourable beaming and weaker central AGN. There does not appear to be a trend in jet-to-core ratio with redshift. For the 30 quasars at $0.2 < z < 2.2$ with detected X-ray jets in the sample of Marshall et al. (2018), the mean and median for this ratio are 3.8 and 2 per cent, respectively. Three sources have a jet-to-core ratio above 10 per cent. These are B1421-490 ($z = 0.662$), B1202-262 ($z = 0.789$) and B1030-357 ($z = 1.455$), all with relatively bright terminal hotspots in X-ray and radio. While the large value of X-ray jet-to-core ratio in PKS J1421-0643 is unusual, the large spread of values over sources does not appear to lend useful diagnostic power related to emission mechanisms to this parameter.

Particularly notable about PKS J1421-0643 is its exponentially falling jet radio spectrum. While jet radio spectral information has been published only for three of the four other quasars, we note from column (7) of Table 6 that they are all steep compared with typical quasar cores. If those jets are similar to PKS J1421-0643 in having a maximum Lorentz factor with a value in the thousands, their radio emission should also plummet at higher frequencies — something that could be tested with higher-frequency radio data.

Column (8) of Table 6 shows that all the sources have jet X-ray spectra consistent with emission from particles that are newly accelerated and have not suffered significant energy losses. This is accommodated easily within an iC-CMB framework, because low-energy electrons are producing the emission. It is unfortunate that such electrons produce their synchrotron emission at very low MHz frequencies, inaccessible to direct observation (see, for example, column (9) of Table 5.

Column (9) of Table 6 gives the jet ratio of monochromatic observer-frame flux density times frequency in the X-ray and radio, as indicative of the relative output in the two bands. The range of only one order of magnitude in this parameter might be taken as indicating a close relationship between the emissions, as is true for an iC-CMB model which relates them through a single electron population, albeit extrapolated to different spectral energies. Equation (8) of Worrall (2009) shows that for the iC-CMB model we expect

$$\frac{\nu_{\rm X} S_{\rm X}}{\nu_{\rm r} S_{\rm r}} \propto \frac{\delta^{1+\alpha}}{B^{1+\alpha}} (1+z)^{3+\alpha} \left(\frac{1+\cos\theta}{1+\beta} \right)^{1+\alpha} . \quad (6)$$

The range of values in Table 6 can easily be accommodated by a combination of the increasing values of z (see Table 1) and small variations in beaming factors and intrinsic magnetic field strength. With large samples it should be possible to use high-redshift sources to construct expectations of the contribution of the iC-CMB mechanism at low redshift and compare with results there, particularly for cases where the iC-CMB mechanism appears ruled out as the main emitter of the X-rays and so predictions should fall below observations.

7 SUMMARY

We have presented new results from *Chandra*, *HST* and the *VLA* for the $z = 3.69$ radio-loud quasar PKS J1421-0643, studying the core and extended jet. We find very steep radio spectra in the extended jet allowing, for the first time in an X-ray-jetted quasar, a maximum Lorentz factor for the radio-synchrotron-emitting electrons to be established. High-resolution radio mapping at lower frequencies would test the predicted spectral flattening to frequencies where the spectrum is expected to reflect that from particle acceleration.

PKS J1421-0643's high redshift makes it a prime candidate for application of the iC-CMB model to the *Chandra*-detected X-ray emission, extending about 4.5 arcsec from the core. The measurement of an X-ray spectral index typical of radiation from newly accelerated particles is consistent with such an interpretation. We have demonstrated that the data follow the expectations of the model for a modest magnetic field strength of a few nT, Doppler factor of about 4, and viewing angle of about 15°. Such parameters imply that the jet extends for about 130 kpc. Under the model, the electrons emitting the highest-energy radio emission need a few separate acceleration regions along the jet, roughly consistent with the level of knottiness and bending that is seen.

Emission plummets in the sub-mm to mid-infrared bands, and at high-energy gamma rays above about 10^{20} Hz, under such an iC-CMB description if there is no additional ultra-relativistic particle population. This creates difficulties for methods used to rule out iC-CMB as the dominant X-ray emission mechanism of some quasar jets at low redshift. We have compared measurements of PKS J1421-0643 with those of the four other $z > 3.5$ quasars with resolved X-ray jets. With sufficiently large samples it should be possible to use modelling at high redshift to predict the contribution of iC-CMB to the X-rays of quasars at low redshift. Such predictions would be expected to be below detected levels in some quasars.

We have discussed the considerable uncertainties in estimating jet power from uncertain jet composition and minimum-energy conditions. If we rely on converging evidence favouring an electron–positron jet, the preferred jet power is of order 3×10^{46} erg s^{-1}, a small fraction of the quasar bolometric luminosity. Only about 0.07 per cent of this jet power is released as radiation, leaving most available for heating the intergalactic medium, and the radiated power ratio is even lower if the jet contains heavy particles. PKS J1421-0643's core X-ray spectrum is typical of other high-redshift quasars, for the majority of which the extended X-ray jet properties are unknown, and variability constrains the emitting region to be less than about 0.7 pc in size. PKS J1421-0643 also falls into the significant group of radio-loud quasars at moderate to high redshift for which the nuclear spectrum shows significant curvature implying intrinsic X-ray absorption of $N_{\rm H}$ a few 10^{22} cm^{-2} if at the redshift of the source.

ACKNOWLEDGEMENTS

Results are based on observations with *Chandra*, the *VLA* and *HST*. We are grateful to the *Chandra* X-ray Center

for its support of *Chandra* and relevant analysis software. The National Radio Astronomy Observatory is a facility of the National Science Foundation operated under cooperative agreement by Associated Universities, Inc. Data from the NASA/ESA Hubble Space Telescope were obtained from the Space Telescope Science Institute (STScI), which is operated by the Association of Universities for Research in Astronomy, Inc., under NASA contract NAS 5-26555. This research has made use of the NASA/IPAC Extragalactic Database (NED), which is operated by the Jet Propulsion Laboratory, California Institute of Technology, under contract with the National Aeronautics and Space Administration. DAS and AS acknowledge support from NASA grant GO8-19085X, NASA contract NAS8-03060 to the CXC, and grant HST-GO-15376.002-A from the STScI. We thank the referee for constructive comments.

DATA AVAILABILITY

The data underlying this work are publicly accessible from https://cda.harvard.edu/chaser/ (*Chandra*), https://archive.nrao.edu/archive/advquery.jsp (*VLA*), and https://archive.stsci.edu/hst/search.php (*HST*) using the identifiers given in the article. Data products arising from the further processing described, and used for the figures shown, are available upon reasonable request to the first author.

REFERENCES

Achterberg A., Gallant Y.A., Kirk J.G., Guthmann A.W., 2001, MNRAS, 328, 393
Arcodia R., Campana S., Salvaterra R., Ghisellini G., 2018, A&A, 616, A170
Asplund M., Grevesse N., Sauval A.J., Scott P., 2009, ARAA, 47, 481
Barthel P.D., 1989, ApJ, 336, 606
Bassett L.C., Brandt W.N., Schneider D.P., Vignali C., Chartas G., Garmire G.P., 2004, ApJ., 128, 523
Bechtold J., Siemiginowska A., Aldcroft T.L., Elvis M., Dobrzycki A., 2001, ApJ, 562, 133
Ben Haim S., Behar E., Mushotzky, R.F., 2019, ApJ, 882, 130
Böhringer H. et al., 2001, A&A, 365, L181
Breiding P., Meyer E.T., Georganopoulos M., Keenan M.E., DeNigris N.S., Hewitt J, 2017, ApJ, 849, 95
Cara M., et al, 2013, ApJ, 773, 186
Celotti A., Ghisellini G., Chiaberge M., 2001, MNRAS, 321, L1
Chartas G. et al., 2000, ApJ, 542, 655
Chartas G., Gupta V., Garmire G., Jones C., Falco E.E., Shapiro I.I., Tavecchio F., 2002, ApJ, 565, 96
Cheung C.C., Stawarz L., Siemiginowska A., 2006, ApJ, 650, 679
Cheung C.C., Stawarz L., Siemiginowska A., Harris D.W., Schwartz D.A., Wardle J.F.C., Gobeille D., Lee N.P., 2008, ASP Conf. Series, 385, 462
Cheung C.C., Stawarz L., Siemiginowska A., Gobeille D., Wardle J.F.C., Harris D.E., Schwartz D.A., 2012, ApJL, 756, L20
Croston J.H., Hardcastle M.J., Harris D.E., Belsole E., Birkinshaw M., Worrall D.M., 2005, ApJ, 626, 733
Dermer C.D., 1995, ApJL, 446, L63
Dickey J.M., Lockman F.J., 1990, ARA&A, 28, 215
Eitan A., Behar E., 2013, ApJ., 774, 29
Ellison S.L., Yan L., Hook I.M., Pettini M., Wall J.V., Shaver P., 2001, A&A, 379, 393
Ellison S.L., Hall P.B., Lira P., 2005, AJ., 130, 1345
Elvis M., Fiore F., Wilkes B., McDowell J., Bechtold J., 1994a, ApJ, 422, 60
Elvis M., et al. 1994b, ApJS, 95, 1
Fabian A.C., Celotti A., Johnstone R.M., 2003 MNRAS, 338, L7
Fruscione A. et al., 2006, Proc. SPIE 6270, "Observatory Operations: Strategies, Processes, and Systems", 62701V
Godfrey L.E.H. et al., 2012, ApJ, 755, 174
Hardcastle M.J., Birkinshaw M., Worrall D.M., 1998, MNRAS, 294, 615
Hardcastle M.J., Birkinshaw M., Worrall D.M., 2001, MNRAS, 326, 1499
Hardcastle M.J. et al., 2016, MNRAS, 455, 3526
Harris D.E. et al., 2017, ApJ, 846, 119
Hogan B.S., Lister M.L., Kharb P., Marshall H.L., Cooper N.J., 2011, ApJ, 730, 92
Hook I.M., Shaver P.A., Jackson C.A., Wall J.V., Kellermann K.I., 2003, A&A, 399, 469
Jester S., Harris D.E., Marshall H.L., Meisenheimer K., 2006, ApJ, 648, 90
Jorstad S.G., Marscher A.P., 2004, ApJ, 614, 615
Jorstad S.G., Marscher A.P., 2006, Astronomische Nachrichten, 327, 227
Kataoka J., et al, 2008, ApJ, 685, 839
Marchenko V., Harris D.E., Ostrowski M., Stawarz L., Bohdan A., Jamrozy M., Hnatyk B., 2017, ApJ, 844, 11
Marshall H.L. et al., 2001, ApJL, 549, L167
Marshall H.L. et al., 2005, ApJS, 156, 13
Marshall H.L. et al., 2010, ApJL, 714, L213
Marshall H.L. et al., 2011, ApJS, 193, 15
Marshall H.L. et al., 2018, ApJ, 856, 66
McKeough K. et al, 2016, ApJ, 833, 123
Meyer E.T., Georganopoulos M., 2014, ApJL, 780, L27
Meyer E.T., Georganopoulos M., Sparks W.B., Godfrey L., Lovell J.E.J., Perlman E, 2015, ApJ, 805, 154
Meyer E.T., Breiding P., Georganopoulos M., Oteo I., Zwaan M.A., Laing R., Godfrey L., Ivison R.J., 2017, ApJL, 835, L35
Miller B.P., Brandt W.N., 2009, 695, 755
Miller B.P., Brandt W.N., Gallagher S.C., Laor A., Wills B.J., Garmire G.P., Schneider D.P., 2006, ApJ, 652, 163
Miller B.P., Brandt W.N., Schneider D.P., Gibson R.R., Steffen A.T., Wu J., 2011, ApJ, 726, 20
Page K.L., Reeves J.N., O'Brien P.T., Turner M.J.L., 2005, MNRAS, 364, 195
Reeves J.N., Turner M.J.L., 2000, MNRAS, 316
Röser H.-J., Meisenheimer K., Neumann M., Conway R.G., Perley R.A., 2000, A&A, 360, 99
Saez C., Brandt W.N., Shemmer O., Chomiuk L., Lopez L.A., Marshall H.L., Miller B.P., Vignali C., 2011, ApJ., 738, 53
Sambruna R.M., Urry C.M., Tavecchio F., Maraschi L., Scarpa, R., Chartas G., Muxlow T., 2001, ApJL, 549, L161
Sambruna R.M., Maraschi L., Tavecchio F., Urry C.M., Cheung C.C., Chartas G., Scarpa R., Gambill J.K., 2002, ApJ, 571, 206
Sambruna R.M., Gambill J.K., Maraschi L., Tavecchio F., Ceruti R., Cheung C.C., Urry C.M., Chartas G., 2004, ApJ, 608, 698
Sambruna R.M., Gliozzi M., Donato D., Maraschi L., Tavecchio F., Cheung C.C., Urry C.M., Wardle J.F.C., 2006, ApJ, 641, 717
Schwartz D.A., 2002, ApJL, 569, L23
Schwartz D.A. et al., 2000, ApJL, 540, L69
Schwartz D.A. et al., 2006, ApJ, 640, 592
Schwartz D.A. et al., 2019, Astronomische Nachrichten, 340, 30
Siemiginowska A. et al, 2003a, ApJ, 595, 643
Siemiginowska A., Smith R.K., Aldcroft T.L., Schwartz D.A., Paerels F., Petric A.O., 2003b, ApJL, 598, L15

Siemiginowska A., Stawarz L., Cheung C.C., Harris D.E., Sikora M., Aldcroft T.L., Bechtold J., 2007, ApJ, 657, 145
Sikora M., Nalewajko K., Madejski G.M., 2020, MNRAS, submitted (arXiv:2004.03606v1)
Simionescu A. et al., 2016, ApJL, 816, L15
Snios, B. et al., 2020, ApJ, in press
Tananbaum H., Weisskopf M.C., Tucker W., Wilkes B., Edmonds P., 2014, Rep. Prog. Phys., 77, 066902
Tavecchio F., Maraschi L., Sambruna R.M., Urry C.M., 2000, ApJL, 544, L23
Tavecchio F., Ghisellini G., Celotti A., 2003, A&A, 403, 83
Tavecchio F., Maraschi L., Sambruna R.M., Urry C.M., Cheung C.C., Gambill J.K., Scarpa R., 2004, ApJ, 614, 64
Tavecchio F., Maraschi L., Wolter A., Cheung C.C., Sambruna R.M., Urry C.M., 2007a, ApJ, 662, 900
Tavecchio F., Maraschi L., Ghisellini G., Kataoka J., Foschini L., Sambruna R.M., Tagliaferri G., 2007b, ApJ, 665, 980
Wilkes B.J., Elvis M., 1987, ApJ, 323, 243
Willingale R., 1981, MNRAS, 194, 359
Worrall D.M., 2009, A&ARv, 17, 1 (arXiv:0812.3401)
Worrall D.M., Birkinshaw M., 2005, MNRAS, 360, 926
Worrall D.M., Birkinshaw M., 2006, in Alloin D., Johnson R., Lira P., eds, Lecture Notes in Physics Vol 693, Springer-Verlag, Berlin, p. 39 (arXiv:astro-ph/0410297)
Worrall D.M., Giommi P., Tananbaum H., Zamorani G., 1987, ApJ, 313, 596
Worrall D.M., Birkinshaw M., Young A.J., Momtahan K., Fosbury R.A.E., Morganti R., Tadhunter C.N., Verdoes Kleijn G., 2012, MNRAS, 424, 1346
Wu J., Brandt W.N., Miller B.P., Garmire G.P., Schneider D.P., Vignali C., 2013, ApJ., 763, 109
Yuan W., Fabian A.C., Celotti A., Jonker P.G., 2003, MNRAS, 346, L7
Yuan W., Fabian A.C., Worsley M.A., McMahon R.G., 2006, MNRAS, 368, 985
Zamorani G. et al. 1981, ApJ, 245, 357
Zhu S.F., Brandt W.N., Wu J., Garmire G.P., Miller B.P., 2019, MNRAS, 482, 2016

APPENDIX A: MULTIWAVELENGTH SPECTRA

Multiwavelength spectra similar to Figure 10 for the other jet regions are shown in Figure A1.

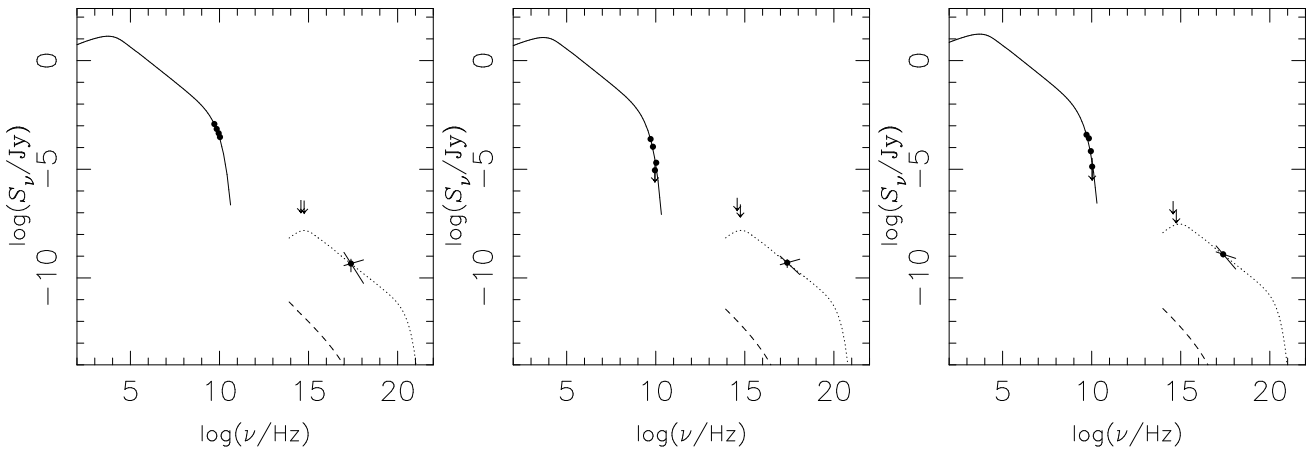

Figure A1. Same as Figure 10 for jet regions A (left panel), B (centre panel) and C (right panel).